

# Passive terahertz camera for standoff security screening

Erich Grossman,<sup>1,\*</sup> Charles Dietlein,<sup>1</sup> Juha Ala-Laurinaho,<sup>3</sup> Mikko Leivo,<sup>4</sup>  
Leif Gronberg,<sup>4</sup> Markus Gronholm,<sup>4</sup> Petteri Lappalainen,<sup>2</sup>  
Anssi Rautiainen,<sup>4</sup> Aleksi Tamminen,<sup>3</sup> and Arttu Luukanen<sup>2,5</sup>

<sup>1</sup>Optoelectronics Division, National Institute of Standards and Technology,  
325 Broadway, Boulder, Colorado 80305, USA

<sup>2</sup>Millimetrewave Laboratory of Finland-Millilab, c/o VTT Technical Research  
Centre of Finland, Tietotie 3, Espoo, Finland

<sup>3</sup>Millimetrewave Laboratory of Finland-Millilab, c/o TKK Helsinki University  
of Technology, Otakaari 5A, Espoo Finland

<sup>4</sup>VTT Technical Research Centre of Finland, Tietotie 3, Espoo, Finland

<sup>5</sup>arttu.luukanen@vtt.fi

\*Corresponding author: erich.grossman@nist.gov

Received 22 December 2009; revised 3 June 2010; accepted 9 June 2010;  
posted 14 June 2010 (Doc. ID 121791); published 28 June 2010

We describe the construction and performance of a passive, real-time terahertz camera based on a modular, 64-element linear array of cryogenic hotspot microbolometers. A reflective conical scanner sweeps out a  $2\text{ m} \times 4\text{ m}$  (vertical  $\times$  horizontal) field of view (FOV) at a standoff range of 8 m. The focal plane array is cooled to 4 K in a closed cycle refrigerator, and the signals are detected on free-standing bridges of superconducting Nb or NbN at the feeds of broadband planar spiral antennas. The NETD of the focal-plane array, referred to the target plane and to a frame rate of  $5\text{ s}^{-1}$ , is 1.25 K near the center of the array and 2 K overall. © 2010 Optical Society of America

OCIS codes: 110.6796, 040.2235.

## 1. Introduction

Practical, real-time imaging in the 100–1000 GHz band is of great interest for the screening of personnel for concealed contraband, particularly the detection of suicide bombers at standoff range. A number of approaches are currently being explored [1], whose relative merits in various specific application scenarios are still unclear. Passive approaches have the advantage of diffuse, natural illumination, the configuration for which human vision and image processing is best adapted. Active sources for these frequencies are not only costly and relatively weak but can introduce image artifacts, such as specular “glint,” that

make image interpretation more difficult. On the other hand, passive approaches require extreme sensitivity. As an example, the design goals for DARPA’s current THz Electronics program, which are well beyond the current state-of-the-art for uncooled, low-noise millimeter-wave monolithic integrated circuit amplifiers and will require major advances in InP high electron mobility transistor (HEMT) and heterojunction bipolar transistor (HBT) performance, call for noise figure of  $NF = 12\text{ dB}$  over RF bandwidths of 15 GHz in the 600–1000 GHz range. This is equivalent to a noise-equivalent temperature difference (NETD, the appropriate measure of sensitivity for a passive imager) of 0.2 K, at a per-pixel integration time of 30 ms. The requirement for passive security screening of personnel in indoor environments is approximately 0.5 K [2]. At 100 GHz, imaging

technology is somewhat more mature, and systems are commercially available from multiple vendors (see ref. [1]). Above 100 GHz, only one passive imager is available commercially [3], operating at 250 GHz by heterodyne downconversion. An imaging system based on superconducting quantum interference device (SQUID)-amplified, transition-edge sensors, and cooled by a 300 mK  $^3\text{He}$  adsorption refrigerator is also under development [4], but the commercial viability of such low temperature sensors for this application remains an open question.

In prior work [5], we have demonstrated this same level of sensitivity (noise-equivalent temperature difference NETD = 125 mK) from extremely simple, easily fabricated and low-cost, hotspot microbolometers. The cost of this sensitivity level is the need for cryogenic cooling to 4 K. Using these microbolometers, in either single-element, 8-, or 16-element array formats, we have obtained excellent imagery by scanning the primary collecting mirror over a target in a slow raster scan [6–8]. The single feature that most distinguishes this microbolometer imagery from other mmw/THz imagery is its extremely broad frequency coverage, nominally 0.2–1.8 THz. It therefore spans a large range in both clothing transmittance [9] and spatial resolution. The full impact of the broad bandpass is beyond the scope of this paper but is indirectly visible in images that include both surface and clothing-concealed features. However, an accurately measured spectral response for the system is still lacking; as described below, indirect evidence from (cryogenically measured) beam patterns does not agree well with earlier, room-temperature photomixer measurements [8].

The goal of the present project has been to increase the speed of the microbolometer imaging to real time (10 frames per second or more) operation, at reasonably low cost, while maintaining comparable image quality. The approach is to assemble 8-element detector modules into a linear, 64-element focal-plane array (FPA), and to combine this with a conical (mechanical) scanner to synthesize an image field of  $\sim 10$  kilopixels. It should be emphasized that this type of scanned architecture provides increased (image) pixel count at the expense of sensitivity. Specifically, the NETD is increased by approximately  $N_{\text{scan}}^{1/2}$ , where  $N_{\text{scan}}$  ( $= 230$ ) is the number of acquisitions per detector per scan. This accounts for most of the NETD difference between prior reports [5] (approximately 100 mK) and that described below ( $\sim 1$  K). For simplicity, the readout of the FPA is done by “brute force,” wiring the 64 independent channels from 4 K to room temperature without any multiplexing. This project presents a sizeable engineering task, involving design and construction of a considerable amount of parallel, low-noise electronics and a significant data throughput. At the same time, significant open questions about detector manufacturing and performance (uniformity, reliability) that could be glossed over while working with small detector numbers are very significant for the larger FPA.

The 64-element camera has been under development since 2006, and a number of progress reports have appeared [10,11] in conference proceedings. This paper attempts to describe its design, the performance of its components, and the current performance of the system, somewhat more comprehensively than before. Two copies of the camera have been built, one at NIST and one at VTT; they are nearly identical in construction and performance. Unless otherwise indicated, the detailed results presented here originate from the NIST system.

## 2. Detectors

Construction of the microbolometers has been described in several prior publications [5,12]; however, the details continue to evolve. Briefly, the antenna is patterned from a bilayer of superconductor (NbN or Nb) and normal metal (Al or Au). The superconducting film lies beneath the normal metal (i.e., against the  $\text{SiO}_2$ -coated Si substrate). At the feed of the antenna, the overlying normal metal is selectively etched away, leaving a small superconducting wire (approximately  $1\ \mu\text{m}$  wide and  $8\text{--}24\ \mu\text{m}$  long, depending on the device version) bridging the antenna's feedpoints.  $\text{SiO}_2$  is deposited to passivate the Nb microbolometers, and in all cases the final step consists of etching beneath the bridge through small windows in the  $\text{SiO}_2$  located on each side of the bridge, thereby releasing the bridge from the underlying substrate. Scanning electron microscope (SEM) micrographs of completed Nb and NbN microbolometers are shown in Fig. 1. Note that the superconductor/ $\text{SiO}_2$  bilayer forming the bridge was in these examples clearly deposited with slight compressive stress, so that upon release, a small out-of-plane curvature was introduced along the bridge length. The Nb microbolometers were fabricated, except for the final micromachining step, at a commercial foundry specializing in superconducting circuits. The NbN microbolometers were fabricated at the in-house facilities of VTT. The thickness and length of the bridge deliberately differs for Nb and NbN bolometers (and in some cases between wafer runs for the same material) in order to maintain reasonable impedance matching to the (nominally  $75\ \Omega$ ) planar antenna, despite the very different (normal-state) electrical resistivities of the two materials.

It is natural and important to compare the performance of various materials that can be used to form

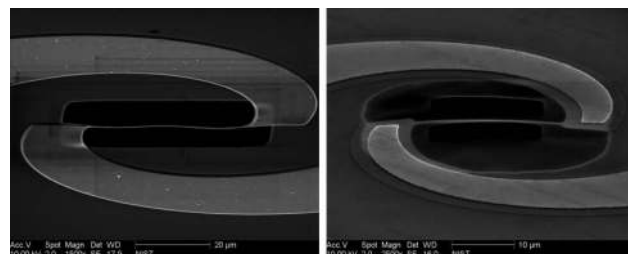


Fig. 1. SEM images of microbolometers used in the camera: (left) NbN with Al antenna and (right) Nb with Au antenna. Note the difference in scales.

the microbolometer and the antenna. Since the preliminary comparison between Nb and NbN microbolometers described in [12], two significant modifications have been made: the antenna material for the Nb microbolometers has been changed from Al to Au, and the stoichiometry of the NbN microbolometers has been changed so as to reduce its superconducting critical temperature ( $T_c$ ), and thereby its saturation power (see below). Despite very substantial differences in geometric and material properties between the Nb and NbN microbolometers (the film thicknesses differ by a factor of  $\sim 5$  for example, and the superconducting penetration depths by a larger factor), the final NETD performance of the two sets of bolometers is identical. This material independence is quite remarkable, and a testament to the robustness of the hotspot microbolometer concept.

#### A. Nominal Hotspot Bolometer

The physics governing the hotspot microbolometers used in this camera was described several years ago [13]. In addition, there is a considerable heritage of other detectors, also modeled as 1-D bolometers at the feeds of planar antennas. In particular, the hotspot microbolometer is closely related to the superconducting, hot-electron bolometer (HEB), often used as a low-noise heterodyne mixer, and to the uncooled resistive microbolometer, often used for antenna diagnostics and other large-signal applications. The 1-D hotspot model of the HEB was given by Merkel [15], and a 1-D model of an uncooled resistive microbolometer was given by Neikirk and Rutledge [16]. All the models begin with a 1-D heat equation. The superconducting hotspot models use two separate differential equations for the superconducting and normal regions, matched at the interface; for the direct detectors employed here, no distinction between electron and phonon temperature is necessary and the model is simply expressed by

$$\begin{aligned} \kappa \frac{d^2 T}{dx^2} + \frac{P_o}{Al_n} + \frac{V^2}{\rho l_n^2} &= 0, & |x| < l_n, \\ \kappa \frac{d^2 T}{dx^2} &= 0, & l_n < |x| \leq l. \end{aligned} \quad (1.1)$$

Here  $\kappa$  and  $\rho$  are the thermal conductivity and electrical resistivity of the bridge, respectively;  $A$  is its cross-sectional area;  $l$  is its overall length; and  $l_n$  is the length of the normal hotspot at its center. The solution of the applicable 1-D heat equation for the superconducting case, for finite optical power is [5]

$$\begin{aligned} I &= V/R_n \left\{ 1 + 2 \left[ (p_o + p_e - 1) \right. \right. \\ &\quad \left. \left. + \sqrt{(p_o + p_e + 1)^2 - 4p_o} \right]^{-1} \right\} \\ &= \frac{V}{R_n} + \frac{P_{\text{sat}}}{V} \quad \text{for } p_o = 0, \end{aligned} \quad (1.2)$$

where  $p_o = P_o/P_{\text{sat}}$  is the optical power normalized to the saturation power  $P_{\text{sat}} = 4\kappa A(T_c - T_0)/l$  and  $p_e = V^2/P_{\text{sat}}R_n$  is the inverse electrothermal loop gain [13]. This model assumes an infinitesimally small width for the superconducting to normal metal transition. The thermal conductivity is assumed to be constant and of equal magnitude in the normal state and superconductive regions, which is a valid assumption at temperatures above 1 K [14] and when only moderate gradients of a few K are present in the bridge. The corresponding temperature profile for the above solution is quadratic within the normal hotspot and linear from the hotspot boundary to the end of the bridge. This solution applies for the case in which the optical power is dissipated entirely within the normal (hotspot) section of the bridge.  $P_{\text{sat}}$  and the normal state resistance  $R_n$  are the two most fundamental parameters describing the microbolometer's construction.

The I-V curves described by (1.2) asymptotically approach an ohmic one with  $\frac{dV}{dI} = R_n$  at high bias, then at lower bias (and for  $P_o < P_{\text{sat}}$ ) pass through a minimum, and then display a region of negative dynamic resistance. The I-V curve in this region would asymptotically approach a hyperbolic form,  $VI = P_{\text{sat}}$ , at low bias, but ordinarily, the hotspot becomes unstable well before this occurs and the I-V curve snaps back to the superconducting branch ( $V = 0$ ). Most actual device I-V curves (Fig. 2) fit this model remarkably well [5,12]. The current responsivity follows directly from (1.2)

$$\begin{aligned} E_I &= \frac{dI}{dP_o} = \frac{-2p_e}{V} \left[ (p_o + p_e + 1)^2 - 4p_o \right. \\ &\quad \left. + (p_o + p_e - 1) \sqrt{(p_o + p_e + 1)^2 - 4p_o} \right]^{-1} \\ &= \frac{-1}{V(p_e + 1)} \quad \text{for } p_o \rightarrow 0. \end{aligned} \quad (1.3)$$

At the minimum of the (dark) I-V curve, the dynamic impedance is infinite,  $V = V_{\text{min}} = \sqrt{R_n P_{\text{sat}}}$ , and  $E_I = -1/2V_{\text{min}}$ .

At a more detailed level, a number of deviations exist from the idealized structure and idealized model that can manifest themselves in observable features. First, local variations in the cross-sectional area of the bridge can exist along its length, resulting, for example, from lithography defects that alter the bridge width, or from minor variations in film thickness. These can be modeled within the context of the same self-heated hotspot formalism, solving the same 1-D heat equation in a piecewise fashion for the regions of different cross-sectional area. The effect on the resulting I-V curves is to introduce a discontinuity in the dynamic resistance  $dV/dI$  at the bias voltage that corresponds to the normal-superconducting (N-S) boundary crossing the discontinuity in cross-section. However, even for large variations in cross-sectional area, the resulting changes in  $I(V)$  are surprisingly small, and as shown in Fig. 3, are often only evident

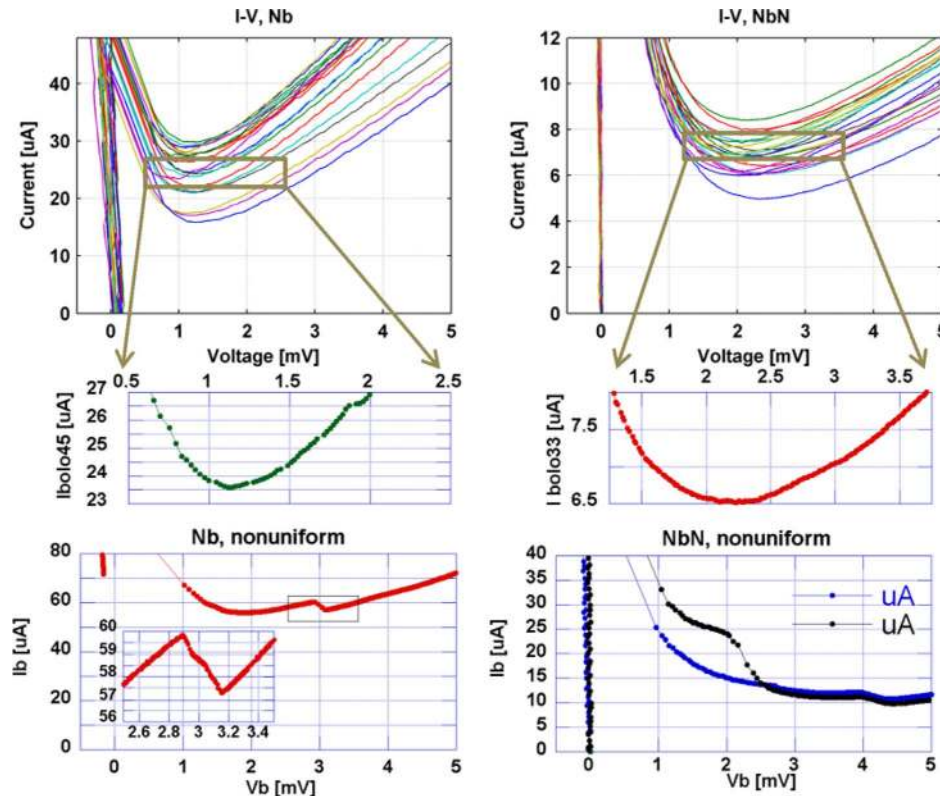


Fig. 2. (Color online) Current–voltage characteristics of Nb (left) and NbN (right) hotspot microbolometers used in the camera’s focal plane array. At the top, 20 I–V curves (for each material) are plotted together to illustrate detector uniformity and large-scale DC properties. At center, the scale of the current axis is greatly expanded near the minimum of current (the operating region), for the median detector in the ensemble. At bottom, I–V curves are shown for individual detectors of each material that exhibit a common type of non-ideal feature.

when the current scale is greatly expanded in the region of the minimum. As shown in the central panels of Fig. 2, the measured I–V curves on both Nb and NbN devices display features similar to this theoretical expectation, when examined on a sufficiently fine scale in the region of the current minimum. The significance of such features from an operational standpoint is not entirely clear, but they appear to affect the sensitivity of responsivity and noise to detector bias, and therefore to affect the gain and noise stability of the camera.

A much more blatant deviation of the I–V curves from nominal behavior is shown in the lower panels of Fig. 2, for both Nb and NbN devices. These deviations have a different qualitative character from those just discussed, and, unlike those, can often appear in a hitherto ideal detector after it has been subjected (accidentally) to high current spikes. The features resemble smoothed discontinuities in current (not in  $dV/dI$ ) and suggest switching between two idealized I–V curves with slightly different values of saturation power. It is natural to speculate that they arise from local variations in  $T_c$  (as opposed to variations in  $A$ ) along the length of the bridge. Figure 3 illustrates theoretical (I–V) curves [from Eq. (1.2)] that appear to simulate the effect reasonably well. The rise in current at lower voltages implies a lower  $T_c$  in the outer regions of the bridge than at the center. The voltage at which the discontinuity appears corresponds to the physical location

of the change in  $T_c$ , lower voltages implying locations nearer the center ( $x/l = 0$ ) and higher voltages implying locations nearer the edge ( $x/l = 1$ ) of the bridge. Remarkably, these features seem to have very little effect on operational performance of the detectors, besides changing the optimal bias point.

As described below, the  $1 \times 64$  FPA is highly modular, each module housing a single chip with a  $1 \times 8$  detector subarray. Two primary FPA configurations have been used for the camera to date, one

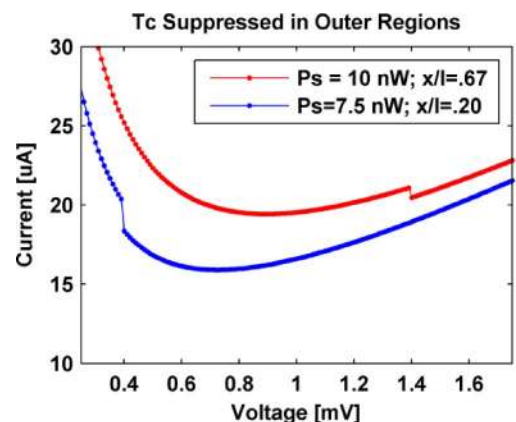


Fig. 3. (Color online) Theoretical I–V curves, from Eq. (1.3), simulating the effect of a 10% reduction in  $P_{\text{sat}}$  (corresponding to  $\sim 0.3$  K suppression of  $T_c$ ) in the outer edges of the bridge. The boundary between the 2 regions lies at a fractional bridge length  $x/l$ .



comprising 7 NbN microbolometer subarrays and one Nb subarray, the other comprising 7 Nb subarrays and one NbN subarray. These configurations were chosen in order to compare performance from the two detector materials in a direct, side-by-side fashion (i.e., in an identical cryogenic environment, with identical target scenes, etc.) The system at VTT employs NbN detectors only. The I-V curves shown in Fig. 2 illustrate typical device properties for each type of microbolometer. Detector uniformity is well illustrated in the top pair of panels and qualitatively appears to be somewhat better in the case of the NbN devices than the Nb. (This is difficult to quantify because several other aspects of both the Nb and NbN devices were modified during the wafer runs that populated the arrays.) This difference, if true, would not be surprising in view of the much lower thickness of the Nb films, nominally 25 nm, compared to the NbN films. Nonuniformity in detector I-V curves translates directly into nonuniformity in channel gain and noise in the array (see Eqn. (1.3) and (1.5) in Section 3). The conical scanning in turn translates these channel nonuniformities into circular artifacts in the final images. Because of the eye's sensitivity to large regular structures, even the superficially modest nonuniformities implied by Fig. 2 (optimistically at the  $\pm 15\%$  level for NbN) translate into extremely prominent rings. Therefore correction of the datastream by the individual channel gains ("flat-fielding," discussed in Section 4) is absolutely essential. The accuracy and stability of this flat-fielding, however, limit the final image quality. To the extent that detector uniformity can be improved, the demands on the accuracy and stability of the flat-fielding are reduced and image quality will be improved.

The modules are mounted directly to a Cu cold finger that also supports a circuitboard containing the interconnects and cold passive components (see Fig. 4). The unit is cooled to a base temperature of 4 K by a commercial pulse-tube cryocooler with a rated capacity of 250 mW. Cryocoolers inevitably introduce some degree of temperature oscillation at their compressor frequency (1.3 Hz in this case), and as described below, this is a source of interference in the array output. However, its impact is greatly reduced by two effects: the substantial thermal mass of the cold finger, IR radiation shields, and array provides a "thermal RC" filter that reduces the temperature fluctuations from  $\sim 0.5$  K to a few mK, and the electrothermal feedback effect in a hotspot microbolometer strongly reduces the sensitivity of device resistance to fluctuations in bath temperature  $T_0$ , when  $T_c - T_0 \gg \Delta T_c$ , where  $\Delta T_c$  is the intrinsic transition width. The electrothermal feedback effect likewise ensures that nonuniformity in  $T_c$  between detectors has very little effect on responsivity, since the feedback "self-regulates" each device's thermal profile about its individual  $T_c$ . Equations (1.3) and (1.5) illustrate this explicitly, showing no strong dependence of current responsivity or noise on  $T_c$  [17].

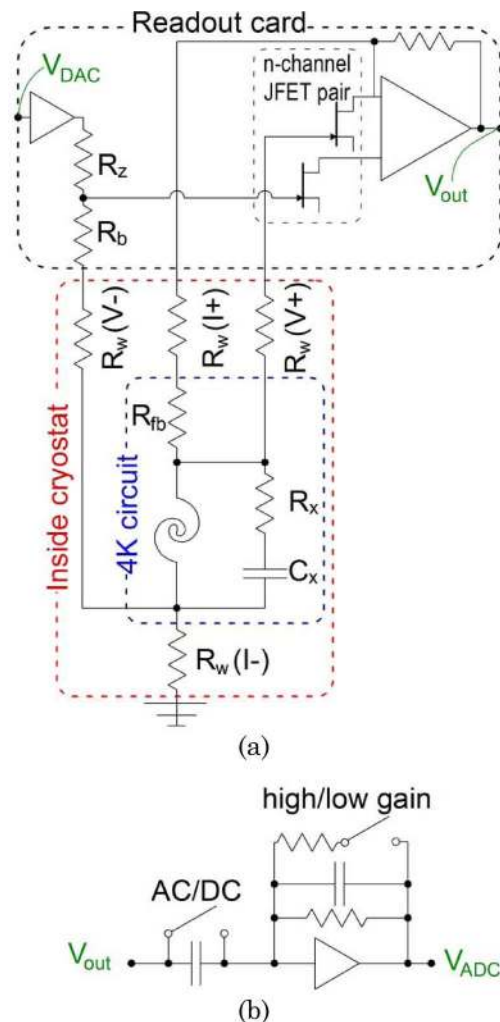


Fig. 4. (Color online) Low-noise transimpedance readout circuit, first stage (upper) and second stage (lower) of a single channel.

## B. Noise

Prior discussions of the hotspot microbolometer have underemphasized a fundamental contrast with zero-dimensional or "lumped" microbolometers, regarding the thermal conductance. This is a key parameter characterizing lumped microbolometers, particularly in regard to their phonon, or thermal fluctuation noise. Phonon noise is the dominant intrinsic noise source of the hotspot microbolometers in practical operation. The classic phonon noise formulas  $S_P = 4kT^2G$  and  $S_T = 4kT^2/G$  describe the power and temperature spectral densities, respectively, due to phonon noise in lumped microbolometers. It is natural, and useful as a rule of thumb, to adapt these to hotspot microbolometers by identifying the effective phonon noise temperature with  $T_c$  and the effective thermal conductance with  $G = P_{\text{sat}}/(T_c - T_0) = 4\kappa A/l$ . However, this is not strictly self-consistent, because the definition of an appropriate temperature and thermal conductance is ambiguous in the case of a hotspot microbolometer, which supports large temperature gradients within its active length. Mather's [18] treatment only partially

addresses this, as it was derived for the case of a distributed thermal resistance but a lumped electrical resistance, whereas the hotspot microbolometer has both distributed thermal and electrical resistances. Clearly, the classic phonon noise formulas must apply for some appropriately defined effective temperature and effective thermal conductance, and using  $T_{\text{eff}} = T_c$  and  $G_{\text{eff}} = 4\kappa A/l$  provides reasonable estimates just on dimensional grounds, but the numerically correct definitions for  $T_{\text{eff}}$  and  $G_{\text{eff}}$  are unclear.

As described above, the array readout is implemented in a “brute-force,” nonmultiplexed fashion, with four wires running from 4 K to room temperature for each detector channel. Electronic readout is performed by a separate 300 K transimpedance amplifier for each channel that presents a virtual short circuit to the detector terminals using active feedback. This approach, detailed by Penttilä [19], is illustrated in Fig. 4. The cold shunt resistor and capacitor ( $R_x$  and  $C_x$ ) maintain the voltage bias at higher frequencies that still lie within the detector bandwidth, but for which the wiring inductance presents too large an impedance for the feedback to be effective. The strength of this transimpedance readout scheme is that it provides excellent noise performance, introducing negligible noise beyond the detector noise when the detector is biased near the minimum of its I-V curve, even though the active electronics is located entirely at room temperature. On the other hand, it does not provide high accuracy for I-V measurements because conversion of the measured voltages  $V_{\text{out}}$  and  $V_{\text{DAC}}$  to device current and voltage depends on accurate values for the wiring resistances  $R_w$ , which are typically not known to better than  $\sim 5\%$ . In addition, the transimpedance gain is proportional to the cold feedback resistance  $R_{\text{fb}}$ . For the standard  $5\text{k}\Omega$  surface-mount resistors used in the camera, there is significant temperature dependence to  $R_{\text{fb}}$  (it is well fit by  $R_{\text{fb}} = R_0 e^{T_s/T}$ , with typical scale temperatures of  $\sim 1.5$  K). This can lead to slow drifts in the gain and variations in gain from cooldown to cooldown and channel to channel.

By design, the noise of the combined detector and readout varies strongly with detector bias [5,11,19]. When the dynamic resistance  $dV/dI$  is sufficiently large, the room temperature amplifier noise  $S_a$  (which can be approximated as almost entirely equivalent voltage noise) is strongly suppressed, and the intrinsic detector noise dominates the output signal. Explicitly, the current noise spectral density can be written as a function of detector bias voltage as

$$\begin{aligned} S_I &= S_a \left( \frac{dI}{dV} \right)^2 + \frac{4kT_{\text{eff}j}I}{V} \left[ \frac{V^4}{(V^2 + V_{\text{min}}^2)^2} \right] + 4kT_{\text{eff}p}^2 G_{\text{eff}} E_I^2 \\ &= S_a \left( \frac{dI}{dV} \right)^2 + \frac{4kT_{\text{eff}j}I}{V} \left[ \frac{V^4}{(V^2 + V_{\text{min}}^2)^2} \right] \\ &\quad + 4kT_{\text{eff}p}^2 G_{\text{eff}} \left[ \frac{V_{\text{min}}^4}{V^2(V^2 + V_{\text{min}}^2)^2} \right], \end{aligned} \quad (1.4)$$

where  $V_{\text{min}} = \sqrt{P_s R_n}$  is the voltage and  $I_{\text{min}} = 2\sqrt{P_s/R_n}$  the current, at the minimum in the I-V curve, and we have used the limiting  $p_0 \rightarrow 0$  form of Eq. (1.3) to substitute for the detector responsivity  $E_I$ . The first term in Eq. (1.4) is the amplifier noise referred to the input, the second term the detector Johnson noise, modified for electrothermal feedback by the term in square brackets, and the third term the detector phonon noise. Measurements of the bias dependence of the noise indeed show a deep minimum at  $V = V_{\text{min}}$ . When the detector is biased at  $V = V_{\text{min}}$ , the amplifier noise contribution vanishes and Eq. (1.4) reduces to

$$S_I = \frac{2kT_{\text{eff}j}}{R_n} + \frac{kT_{\text{eff}p}^2 G_{\text{eff}}}{R_n P_s} = \frac{2kT_{\text{eff}j}}{R_n} + \frac{kT_{\text{eff}p}^2}{R_n(T_c - T_0)}. \quad (1.5)$$

The second form of Eq. (1.5) uses the non-self-consistent effective thermal conductance  $G = P_{\text{sat}}/(T_c - T_0) = 4\kappa A/l$  mentioned above. The effective temperatures for Johnson and phonon noise are not necessarily equal to one another or to  $T_c$ . The effective temperature for Johnson noise should be simply the mean temperature within the normal hotspot, and this can be readily calculated from the temperature profile to be  $T_{\text{eff}j} = T_c^2/(T_c - T_0)$ , which for typical values of  $T_c = 7$  K and  $T_0 = 4$  K leads to a Johnson noise contribution close to  $S_I(\text{Johnson}) = 2kT_c/R_n$ .

Figure 5 displays the current noise spectrum of two typical detectors, one Nb and one NbN, when biased at the minima of their respective I-V curves, while table 1 summarizes relevant parameters. A 5 kHz low-pass filter has been applied to the input data prior to Fourier transformation. The normal resistances are obtained from fits of (the full form of) Eq. (1.2) to the measured I-V curves; we estimate them to be accurate to  $\pm 10\%$ . The critical temperature for both materials is  $7 \pm 0.5$  K. The measured current noise listed is the median noise spectral density in the 100–1000 Hz band, which accurately represents the white noise in the most relevant frequency band for the camera. There is a small but significant discrepancy between the measured noise and the simple  $S_I = 4kT_c/R_n$  expression, amounting

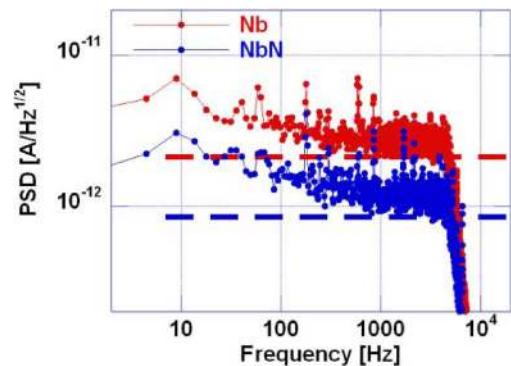


Fig. 5. (Color online) Current noise spectral densities for typical detectors of each material, at their optimal bias points.

to a 40–50% excess in power spectral density (PSD). Although a thorough study requires more attention to gain calibration and more accurate extraction of device parameters, we believe the discrepancy is real and represents the effect described above, namely effective temperatures for the phonon noise and Johnson noise in the hotspot bolometer that are somewhat elevated above  $T_c$ . The last column in Table 1 lists the integral of the noise spectrum, referred to the system output, i.e.,  $\sigma^2 = R_t^2 \int_0^\infty S_I df$ , where  $R_t = 395 \text{ k}\Omega$  is the transimpedance gain. This is simply the rms noise of the output voltage.

### 3. Optical Performance

#### A. Module Optics

The construction of the  $1 \times 8$  detector modules is illustrated in Fig. 6. Optical coupling is based on the classic substrate lens configuration originally developed by Rutledge [20]. High resistivity (to minimize free-carrier absorption loss for 300 K testing) Si lenses are squeezed against the back side of the detector die, and the incoming THz radiation is coupled through the detector substrate onto the lithographic antenna patterned on the front side. The antenna, a self-complementary equiangular spiral, has been described in prior publications and its patterns presented at selected frequencies, as measured with the bolometer at room temperature [21,22]. For substrate-lens coupling, the antenna beams are significantly affected by the extension length  $L$ , the distance from the center of lens curvature to the antenna plane. The hyperhemispherical configuration,  $L = R/n$ , provides higher Gaussicity and is aplanatic (zero coma and spherical aberration), while slightly larger extension lengths,  $L \approx 1.4R/n$ , approximate an elliptical lens and provide higher directivity. The patterns measured at 95, 238, and 650 GHz on the 4 mm elliptical lens [21] indicated a beamwidth in degrees of  $\text{FWHM} = 4.5 \text{ THz} - \text{deg}/f$ , and based on the smaller lens aperture of the  $1 \times 8$  module, the beams from the camera FPA are expected to roughly follow  $\text{FWHM} = 9 \text{ THz} - \text{deg}/f$ , despite changing to a nearly hyperhemispherical configuration ( $L = 1.1R/n$ ) for the 2 mm lenses in the  $1 \times 8$  module. Indeed, the measurements performed at 654 GHz [22] on the 2 mm lenses show a beamwidth almost exactly double that measured for the 4 mm lenses ( $13^\circ \pm 1^\circ$  versus  $6.8^\circ \pm 0.1^\circ$ , where the range indicates variation between orthogonal planes). One such measured pattern is shown in Fig. 7.

However, the measurement that is most directly relevant to camera performance, is that illustrated

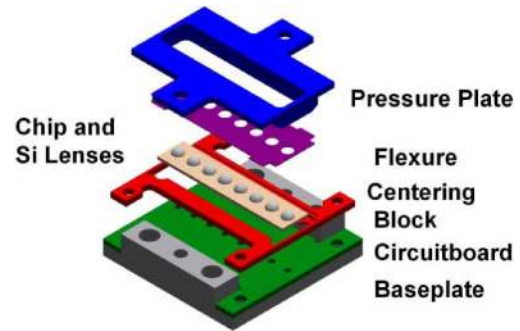


Fig. 6. (Color online) Exploded view of  $1 \times 8$  detector module.

in Fig. 8, in which a broadband blackbody source is scanned through the antenna beam while the detector array is operated cryogenically, at its correct bias condition. Compared to the pattern measurements more typically done for antenna studies, this measurement averages over both polarizations and over a very broad frequency range, limited only by the Zitex IR blocking filters in the cryostat. Beams from 24 separate detectors, in four modules, were measured in this way; results from one module are shown at the top of Fig. 9. In general, the measured main beams are highly circular, and very consistent from detector to detector. Gaussian fits were made to each detector's beam. As shown at the lower right, however, a single Gaussian is only a mediocre fit to the measured pattern of any detector's beam. The deviations from a Gaussian (i.e., the residuals to the fit) are also extremely consistent from detector to detector; the measured beams being invariably stronger than the best-fit Gaussian on axis, and on a ring at approximately  $14^\circ$  off-axis, and weaker than the best-fit Gaussian at intermediate off-axis angles. The full width half-maxima of the fitted beams are  $14^\circ \pm 2.5$ , remarkably close to the monochromatic, single-polarization measurement [22] at 654 GHz. Based on the rough expectation of  $\text{FWHM} = 9 \text{ THz} - \text{deg}/f$ , the measured beamwidth indicates an effective mean frequency of the blackbody response of 640 GHz. This is notably different from the frequency response inferred from a swept photomixer measurement [8], a discrepancy that is not yet understood. It should be noted that the sense of the

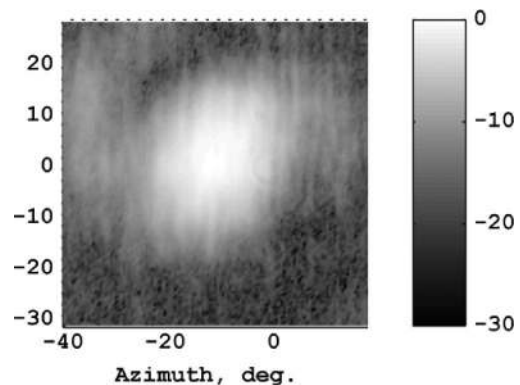


Fig. 7. Monochromatic 654 GHz antenna pattern, measured at 300 K (at VTT). Grayscale is in dB.

Table 1. Noise Parameters of Typical Nb and NbN Microbolometers, Measured at Their Optimal Bias Points

	$R_n$ [ $\Omega$ ]	$\text{Sqrt}(4kT_c/R_n)$ [pA/Hz $^{1/2}$ ]	Median $S_I$ [pA/Hz $^{1/2}$ ]	RMS (output) [ $\mu$ V]
Nb	85	2.1	2.9	81
NbN	550	0.84	1.3	36



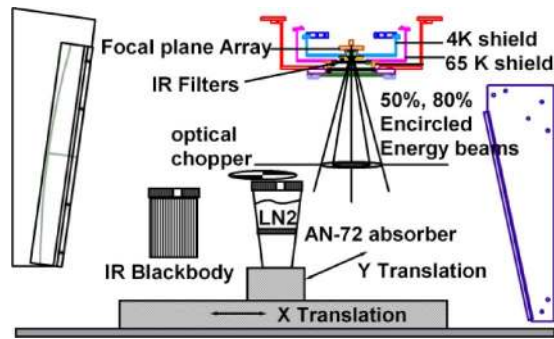


Fig. 8. (Color online) Experimental configuration for measurement of broadband antenna pattern.

deviations from a single Gaussian is that which is expected from a superposition of Gaussians of varying widths, the wider widths corresponding to lower frequencies in the detector response, the narrower widths to higher frequencies. The deviation of the patterns from Gaussian form is thus a natural consequence of the broadband nature of the system response and has little effect on system performance as long as the efficiency for illuminating the optics is high.

Given the good circularity of the beams, it is useful to azimuthally average the data from the beam maps and display it either as an averaged radial beam profile or its integral, an encircled energy plot. The latter is shown in Fig. 10. The angular subtense of the flat secondary mirror (see Fig. 12) that lies just outside the window is  $24^\circ$  in the cross-array direction, and varies in the array direction from  $58^\circ$  at the array center to  $26^\circ$  at the array edge. The  $24^\circ$  width in the worst-case direction corresponds to an encircled energy of  $\sim 75\%$ . Although beam tilt could certainly degrade the performance, the measurements of

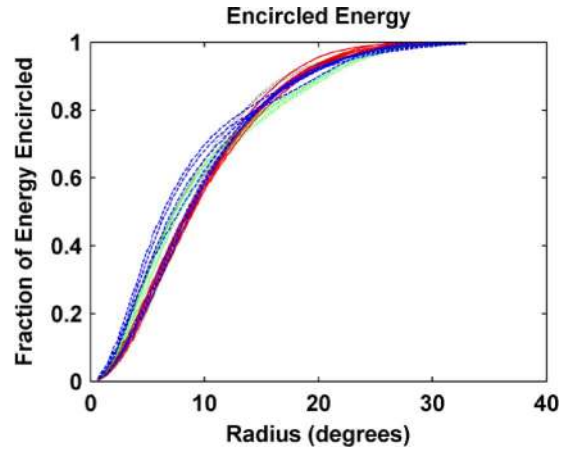


Fig. 10. (Color online) Encircled energy plot for 24 detectors from 4 modules (separate modules, color-coded online).

Fig. 10 indicate that the secondary mirror is reasonably sized, allowing no more than  $\sim 25\%$  spillover if beam tilt is small. Of course, spillover is likely to be somewhat worse at the array edge than the center. The size of the secondary represents a trade-off between this antenna spillover loss and simple beam obscuration.

Measurements of beam tilt are shown in Fig. 11. The chief source of this tilt is imperfect alignment of the substrate lens with the feedpoint of the antenna on the detector die. This is immediately evident from the clustering of the beam tilts by module, and the fact that the largest tilts arise from detectors at the edge of a module. The largest beam tilt is approximately  $9^\circ$ , which corresponds to a physical misalignment of a hyperhemispherical lens of

$$x = R(1 + 1/n) \sin(\theta/n) \approx 60 \mu\text{m}. \quad (1.6)$$

(This follows simply from Snell's law, though detailed simulations and measurement were described in [23].) The lens radius is  $R$ , and its refractive index is  $n$ .) As indicated in Fig. 6, the Nb detector die are aligned to the lenses only through the carefully toleranced dimensions of the centering block (conventionally machined) and the flexure (lithographically fabricated). The NbN detector die have circular micromachined pockets etched into their back side for alignment of the lens. As described in [22], the maximum beam tilts are very similar for the two alignment methods and fully consistent with the  $9^\circ$  value found here. This misalignment will of course vary with each assembly and disassembly of a module. As mentioned above, large misalignments could have a significant impact on the beam illumination of the secondary mirror (and thus the spillover efficiency), particularly for detectors at the edge of the array. Gain measurements made at the target plane (see below) indeed indicate significant efficiency loss at the edge of the array. However, the modular design of the focal plane allows for a simple modification that would improve the efficiency of the beam illumination: the antenna beams of the

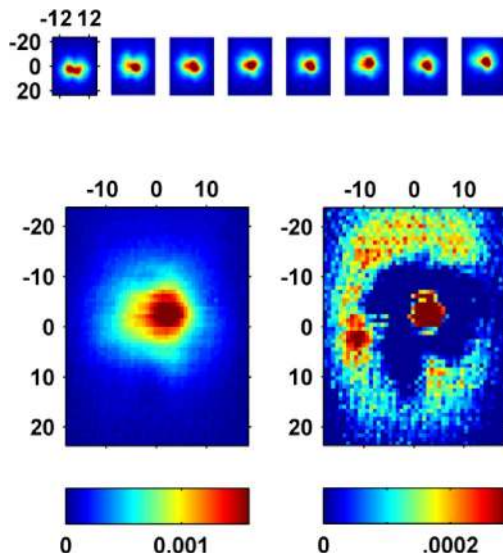


Fig. 9. (Color online) Broadband antenna patterns measured on a Nb detector module. At top, comparison of the 8 individual patterns, plotted on the same scale ( $x$  and  $y$  dimensions in degrees). At bottom left, a single pattern at an expanded scale, and, at right, residual from the best Gaussian fit to it.



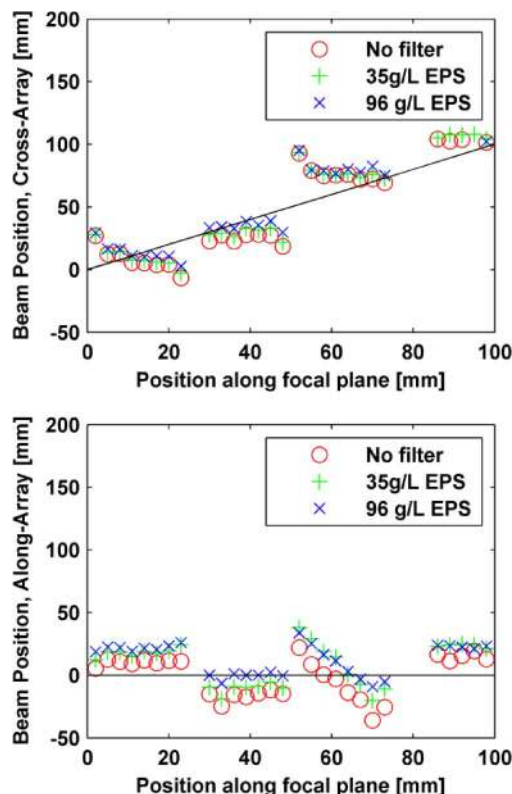


Fig. 11. (Color online) Measured beam locations in the directions orthogonal to (upper) and parallel to (lower) the FPA, for versus detector location in the focal plane.

outermost modules can be deliberately steered toward the secondary mirror, either by building a piecewise concave cold finger for mounting the modules, or by deliberately offsetting the substrate lenses of the outermost modules. The work of [23] indicated that very substantial beamsteering angles,  $\sim 30^\circ$ , much more than is needed in this case, are possible by this technique, without significantly compromising beam quality.

#### B. Conically Scanned System Optics

The overall optical design of the system has been described in a prior publication [24] and is based on an all-reflective off-axis Schmidt telescope. Because full system ray traces indicate that the optimal 6th-order polynomial corrector only provides minor improvements in spot size at the longer wavelengths in our band, the system presently incorporates a flat mirror in place of the corrector. A second minor change has been made, to the orientation of this mirror, in order to provide a viewing angle that is horizontal. This allows the system to be mounted on the floor, level with the targets to be surveilled, a much easier configuration to arrange than the  $8^\circ$  lookdown angle originally planned.

The original system specification called for a FOV of  $4\text{ m} \times 2\text{ m}$  (horizontal  $\times$  vertical) at the nominal target distance of 8 m, equivalent to  $28^\circ \times 14^\circ$ . Conical scanning is a natural technique for covering large fields of view at high speed with the comparatively small number of detector channels in a linear

array. It is therefore widely used in the millimeter-wave imaging community [1,25,26]. A mirror or lens located in an aperture plane is rotated in such a way that the image of each detector traces out a circular path in the target plane. Each rotation of the scanner corresponds to one frame of the camera. Because the mechanical motion is rotational, it can be accomplished much faster than the reciprocal (i.e., “flapping”) motion needed for a raster scan.

However, it is inherent in the nature of conical scanning that the sampling of the target plane is highly nonuniform, with samples spaced very densely at two edges of the FOV (the edges parallel to the array direction) and relatively sparsely at the center of the FOV. In our implementation, the magnification of the Schmidt optics at 8 m range is 10.7. This implies that the sampling interval in the array, i.e. cross-scan, direction (horizontal at the center of the FOV) is 32 mm, the 3 mm spacing of the detectors in the focal plane, times the magnification. Between modules however, the detector spacing is 4 mm, so the maximum cross-scan sampling interval is 43 mm. In the scan direction (vertical at the center of the FOV), the timing is arranged, as described in the next section, to provide a sampling interval of  $(\pi \times 14^\circ)/230 = 0.19^\circ$ . At the top and bottom edges of the FOV, the sampling is of course much denser. The nonuniformly sampled data is eventually interpolated by the display computer to a uniform  $64 \times 128$  pixel image grid, with each image pixel covering  $0.2^\circ \times 0.2^\circ$  ( $3\text{ cm} \times 3\text{ cm}$  at 8 m), as also described in Section 4. The (rather primitive, but fast) interpolation algorithm averages over all samples within a radius of  $0.25^\circ$  from the desired display point. This radius slightly exceeds the *maximum* distance from anywhere in the target plane to the nearest sample point, i.e., it is half the quadrature sum of the in-scan and cross-scan sample intervals. If the averaging radius were significantly smaller, “holes” would be created in the target plane, where no sample points exist within the averaging radius, and a more sophisticated interpolation algorithm would be necessary. A summary of these spatial sampling quantities is

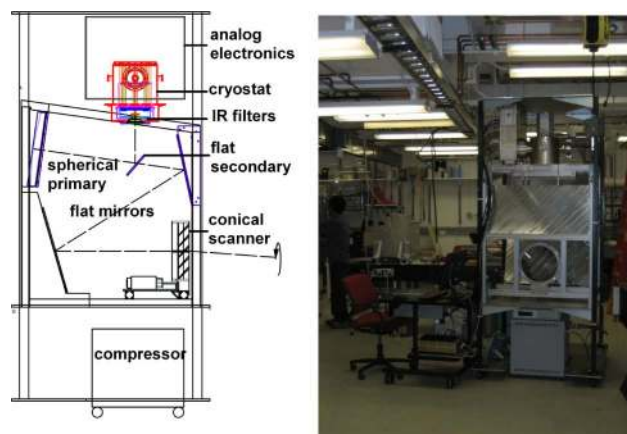


Fig. 12. (Color online) Physical layout of the overall system and a photograph of the assembled system at NIST.

Table 2. Spatial Sampling

	Linear Distance at 8 m (mm)	Angular Distance (Degrees)
Cross-scan interval (typical)	32	0.23
Cross-scan interval (maximum)	43	0.31
In-scan interval	27	0.20
Maximum distance to sample point	25	0.18
Diffraction spot (at 300 GHz) diameter	25	0.18
Interpolation radius	35	0.25
Display grid interval	31	0.22

given in Table 2, along with the standard diffraction-limited spot size,  $\lambda(f/D)$ , at 300 GHz, and the mean measured spatial resolution described below. (Here  $f$  is the 8 m target range, and  $D$  is the 325 mm aperture diameter.) Depth of field, also a very important quantity in practical applications, would be  $\text{DOF} = \lambda(f/D)^2 = 0.6$  m in a completely diffraction-limited system. In this case, where the sampling and interpolation degrade the spatial resolution by a factor of  $\sim 2$  (Table 2), the DOF should be increased (improved) by the same factor.

In order to measure the system point spread function we used a very bright point source that was manually scanned across the system FOV at a distance of 5 m from the conical scanner aperture. This reduced focal distance (from the design focal distance of 8 m) was obtained by refocusing of the system, translating the focal plane away from the primary by 40 mm. The source was a 10 mm diameter, 6 cm long SiC heater (“Globar”), whose filament region (about 1 cm long, 1 cm diameter cylinder) was heated to about 1000 °C. The channel-wise variations in gain were normalized by carrying out a calibration on two NIST ABC blackbody sources, scanned across the FOV. While scanning the heater across the FOV, a THz movie was acquired at 6 fps. In this measurement, the two edge-most modules on the focal plane array were left unbiased, resulting in a laterally reduced FOV with a hole in the middle (corresponding to the scan paths of the above-mentioned four modules). In the data analysis, we carried out frame-by-frame fitting of an ellipsoidal Gaussian, characterized by its amplitude, the full widths at half-maximum of the minor and major axis, as well as centroid location. A Nelder-Mead simplex method [27] was used for a best fit with an initial guess for the centroid position given by the location of the brightest pixel within each frame. Frame-to-frame (temporal) continuity was enforced by applying a radial distance weighing function, which reduced the possibility of erroneous initial guesses for the centroid location.

The fitting routine provided a set of FWHM values (801 in total across the usable FOV) for the major and

minor axis of the ellipsoidal Gaussians. The minor axis value gives a more realistic estimate for the resolution, given that the tubular Globar will also heat along its length and thus appear slightly elongated. A histogram can be used to interpret the camera angular resolution, as shown in Fig. 13. The mean and median of the distribution are 0.67° and 0.64°, respectively, while the peak is located at 0.56°. At 5 m, these values correspond to spatial resolutions of 58 mm, 56 mm, and 48 mm, respectively. The accuracy of the method was estimated by repeated measurements and is estimated to be better than 15%.

When, as here, interpolation is made to a uniform grid that matches the *minimum* sampling density, then the spatial resolution should roughly match the interpolation grid, and the signal-to-noise ratio is improved (by averaging) in regions of denser sampling. If the interpolation were made to a finer grid, then the spatial resolution in the densely sampled regions would be improved, but statistical correlations in the noise would be introduced in the less densely sampled regions. A full discussion of the effects of sample nonuniformity and sparsity on image quality, in the context of conical scanning, is well beyond the scope of this article, not least because “image quality” is a somewhat ill-defined concept for these applications.

The conical scanner employs a “periscopic” design that reflects each incident ray twice off a series of wedged vanes, once off the front of a vane and once off the back of the neighboring vane. The scanner is mounted and driven on its rim, eliminating any central obscuration due to an axle. Basic properties of the scanner are listed in Table 3. The optical efficiency predicted from a full system ray trace is 29%, averaged over the 64 detectors. The efficiency of the scanner is  $\sim 55\%$ , slightly lower than the geometric efficiency (63%) applicable for on-axis, collimated light.

The present sampling of the target plane is considerably too coarse in the center of the field, leading to inadequate spatial resolution for many of the

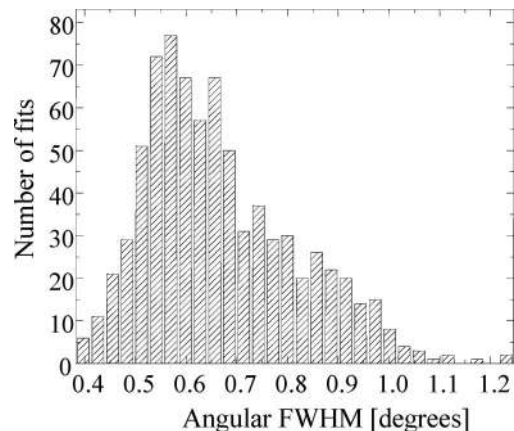


Fig. 13. Histogram (measured at VTT) of the fitted minor axis FWHMs across the FOV, with a mean and median of 0.67° and 0.64°, respectively. The peak of the distribution is at 0.56°.

Table 3. Scanner Properties

Clear aperture diameter	325 mm
Wedge angle	3.56°
Deflection angle	7.125°
Fractional area blocked	15%
Fractional area reflected	22%
Geometric efficiency	63%
Maximum framerate	20 fps (1200 rpm)

personnel screening applications envisioned. Initial system specifications on the focal plane spacing, FOV, and antenna pattern were frozen at the start of the project on values that were in fact inconsistent. In remedying this, the decision was made to adjust the magnification to maintain the original FOV, at the expense of sampling. Fortunately, relatively simple modifications exist that permit recovery of finer sampling and therefore spatial resolution. First, simply doubling the acquisition rate would halve the in-scan sampling interval to 0.10° (Table 2). Second, the modular nature of the focal plane permits simple addition of a second row of detector modules, parallel to the present one but staggered by half the detector spacing. This more than doubles the sampling frequency in the cross-scan direction, reducing the sampling interval to 0.11°. Together these allow for an interpolation radius as small as 0.08°. A 2 × 64 array would maintain the present FOV, while a 2 × 32 array would reduce it but maintain the current detector count. Finally more sophisticated interpolation would provide resolution below the radius of a simple averaging disk. The acquisition system's software is easily able to compensate for the timing offset between the signals from the two rows. Data throughput would increase from the higher acquisition rate.

#### 4. Imaging Performance

In order to translate the incoming datastreams from the analog readout electronics to a usable sequence of displayed or saved images, a relatively sophisticated timing and data acquisition system is needed, and has been implemented as shown in Fig. 14. A pair

of commercial 1 Msample/s, 32 channel, PCI data acquisition cards, mounted in the chassis of a dedicated server, receive the analog outputs of the 64 readout channels over conventional SCSI cables. Separately, two encoders (denoted “shaft” and “tab” encoders) provide timing pulses to the acquisition system. The shaft encoder is mounted to the motor shaft, and provides 230 pulses per frame; datapoints are synchronized to each of these pulses, providing a raw datastream of 230 datapoints × 64 channels × F frames per second. (The somewhat arbitrary choice of 230 scan angles per frame is based on the desire for approximately equal sampling intervals in the scan and cross-scan directions of the field.) The tab encoder is mounted to the scanner body and provides one pulse per frame, thereby fixing the registration of the datastream to the scanner orientation. The acquisition cards are run at their maximum sample rate, 31.25 ksamples/s/channel, and the data samples, as well as the timing pulses, are time stamped by the card's onboard 80 MHz clock. The data samples and timestamps corresponding to a single frame are then placed on a FIFO queue. The number of samples that corresponds to a single frame does of course drift slightly as the instantaneous scanner speed varies, so the acquisition system monitors this and continuously varies the number of samples loaded, so as to prevent the queue from slowly “falling behind” the datastream. A separate, asynchronous part of the acquisition system reads data off the queue, averages the data samples over time intervals corresponding to each scan angle, and arranges the data into a 64 channel × 230 scan angle array, with a header containing a single timestamp for the frame. It also displays selected portions of the incoming data in real time. The acquisition system is implemented in LabView.

The server acquisition system also applies three software filters to each channel's data stream. First, a conventional infinite-impulse response (IIR) low-pass filter, generally set to a 3 dB frequency of 5 kHz and a 6-pole roll-off, is applied, mostly to suppress very high frequency interference aliased into the

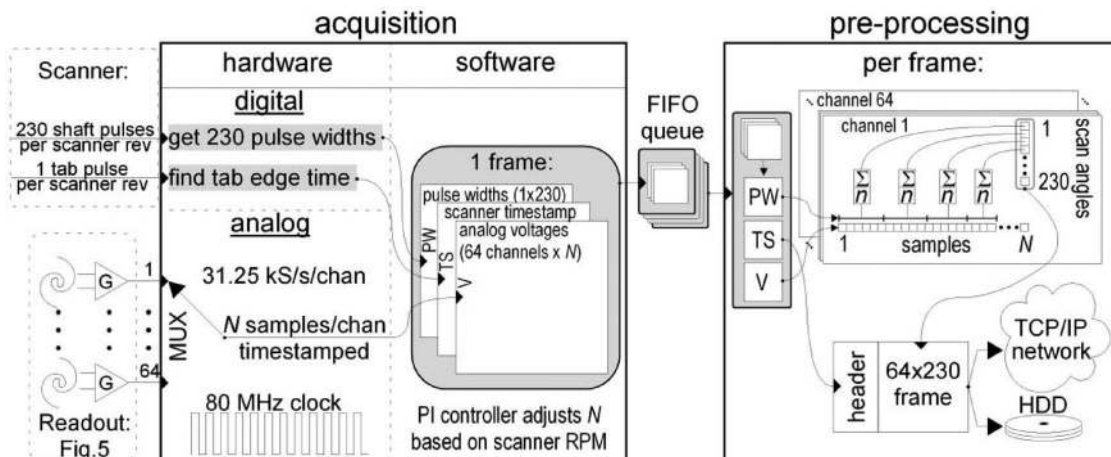


Fig. 14. Block diagram of the timing and data acquisition system.



signal band by the 15.6 kHz Nyquist frequency. A 60 Hz IIR notch filter can also be applied, though in many circumstances it is unnecessary and can be turned off. Finally, and most importantly, some type of low frequency filtering is required to remove residual 1.3 Hz compressor fluctuations. These are due to residual temperature fluctuations (at the mK level) of the cold finger during the compressor cycle. Due to the large thermal mass of the cold finger, their amplitude is much smaller than that of a bare, unloaded cryocooler head, and their form is highly sinusoidal. Their amplitude is still several times larger than typical signals from passive scenes. Although both simple IIR filters and subtraction of the signal from a “dummy” unilluminated pixel were explored, we have found the simplest and most effective filter scheme is for the server to perform a least-squares fit of each frame’s data to a 1.3 Hz sinusoid and then to subtract this fit from the datastream.

The output data (14,720 datapoints  $\times$  16 bytes/datapoint = 240 kB/frame) from the server is then sent to a file on the local hard drive, or to a TCP/IP network connection. The latter feature allows the raw data to be streamed in real time to one or more client computers for remote display, storage, or image processing (limited of course by the speed of the network.) This is exceedingly useful in the lab, as it allows a laptop client computer, connected to the server over an Ethernet cable, to take the place of a human technician stationed at a fixed display computer.

In order to obtain a basic NETD profile across the array, as shown in Fig. 15, the output from the server is recorded under two conditions. First, the data is recorded, typically for 100–200 frames, with a sheet of room-temperature, millimeter-wave absorber fixed in front of the scanner aperture. For each channel, the rms variation in output voltage is calculated over all scan angles and all frames. Then a second dataset is recorded while a large reference source is scanned horizontally across the FOV, near the nominal target distance of 8 m. In some cases, an aqueous blackbody calibration (ABC) source [28],

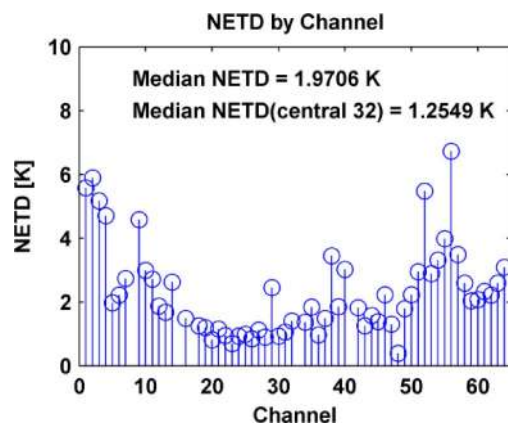


Fig. 15. (Color online) NETD (referred to the target plane) of individual detectors across the array, referred to the 5 fps frame rate.

with an output aperture of 20 cm  $\times$  20 cm, is used as the reference source. In other cases a source made from liquid-nitrogen cooled absorber, with an aperture of 35 cm  $\times$  35 cm is used. The source must be large enough that, even if the source is located somewhat outside the camera’s focal depth, all light incident on a given detector, through the camera’s entrance aperture, originates from inside the source. For each channel, the maximum signal excursion is extracted from this file, corresponding to the signal when the source image is scanned across the corresponding detector. This establishes the (radiometric) temperature responsivity, in V/K, of each channel, referred to the target plane. The ratio of the rms fluctuations from the first dataset to the responsivity from the second dataset directly provides a channel-by-channel NETD, on a per-frame basis, for the particular frame rate used for the noise data acquisition.

As shown in Fig. 15 for a framerate of 5 fps, the NETD is clearly lower near the center of the array than near the edge. The median NETD of the central half of the array is 1.25 K, while the median NETD of the full array is 1.97 K. As explained above, the most likely explanation for this is somewhat worse spillover loss at the secondary mirror for detectors near the edge of the array, particularly in view of a potentially sizeable beam tilt from the detectors. Two other points are notable. First, and quite remarkably, the overall NETD performance of Nb and NbN detectors is indistinguishable. The NbN module in this array occupies channels 25–32, and its NETD is identical to that of its Nb neighbor, occupying channels 17–24. The noise of the NbN detectors is approximately half that of the Nb detectors (Table 1), but their responsivity is also approximately half that of the Nb devices. As seen in the I-V curves (Fig. 2), this is primarily due to lower electrical reponsivity (i.e., higher  $V_{\min}$ ) of the NbN devices but is probably also affected by a slightly poorer impedance match between the NbN devices and the antenna. Secondly, there are generally a few outliers, or “hot” channels, in the array. In most cases, we have found that these are detectors whose noise is unusually sensitive to bias. By re-optimizing the bias, their NETD can be lowered to that of the rest of the array, but because of inevitable small drifts in the bias electronics (arising chiefly from temperature-induced drifts in the FET offsets,) their NETD does not stay as stable as most of the detectors. Because the amplifier noise is very sensitive to  $dV/dI$ , it is natural to speculate that these are detectors that happen to have small discontinuities in  $dV/dI$  near the minimum in the I-V curve. Generally, the noise of the NbN detectors seem less sensitive to the exact bias point, which is likely explained by the much larger film thickness in comparison to the Nb detectors. It should be noted that because the bias electronics is fully automated, autotuning algorithms that periodically readjust the bias to maintain optimum NETD can easily be implemented and could be completely transparent to the user. Finally, the measured NETD level, though

usable, is still approximately a factor of  $3\times$  higher than our design goal of 0.5 K.

In order to arrive at meaningful images, the data needs to undergo a coordinate transformation, from data coordinates of (channel, scan angle) to image coordinates of  $(\theta_x, \phi_y)$ . The image space constitutes a  $128 \times 64$  pixel, uniformly sampled grid, corresponding to a FOV covering  $-15.2^\circ < \theta_x < 15.2^\circ$  and  $-7.5^\circ < \phi_y < 7.5^\circ$ . Performing this transformation is the primary purpose of the display program, which runs concurrently on the client computer, and is implemented in Matlab. The transformation reflects the conical scanning geometry and is highly nonlinear and not even 1-to-1, as is clear by considering the center of the image field, where datapoints from one edge of the array at scan angle  $90^\circ$  overlap with datapoints from the opposite edge of the array at scan angle  $270^\circ$ . (Scan angle  $0^\circ$  is defined as pointing upward, and the scan direction is clockwise as viewed in the images.) Such nonlinear interpolations are simple to implement with high accuracy in high-level languages that utilize sophisticated algorithms. Unfortunately, we found that these implementations are much too slow to keep up with the datarates coming from the server, at least for the relatively modest laptop computer we typically use as a client. A much faster client computer would eliminate this problem, but would largely defeat the purpose of the client-server architecture, which is to allow data display and analysis on any convenient computer connected to the network. Therefore we have implemented our own algorithm, as a simple linear transformation

$$M_{ij} = \sum_{m,n} W_{ijmn} D_{mn} \quad (1.7)$$

where  $M_{ij}$  represents the image pixel values for coordinates  $(\theta_i, \phi_j)$ ,  $D_{mn}$  represents the incoming datapoint for the  $m$ th channel and  $n$ th scan angle, and the weight array,  $W_{ijmn}$ , incorporates all the information about the scanning geometry. The weight array is separately calculated and stored prior to any data collection. Since the coordinate transformation algorithm affects both the spatial resolution and the noise of the resulting image, judicious selection of these weights is important. The information about the scanning geometry originates in the output files of the ray tracing simulation done as part of the optical system design. The ray trace simulation provides, for each channel and each scan angle, the location  $(\theta_{mn}, \phi_{mn})$ , spot size, and efficiency of the best-focus image in the target space. For each image pixel location  $(\theta_i, \phi_j)$ , these detector image locations are sorted in order of increasing Cartesian distance from the desired image point,  $R = \sqrt{(\theta_i - \theta_{mn})^2 + (\phi_j - \phi_{mn})^2}$ . The datapoints corresponding to the closest  $N$  images are then averaged, i.e., assigned weights of  $1/N$  each. The value of  $N$  is the number of image points lying within  $0.25^\circ$  of  $(\theta_i, \phi_j)$ , or 8, whichever is fewer. Thus in areas of

the field where datapoints are densely packed (for example, near  $\theta_x = 0$  and  $\phi_y = \pm\phi_{\max}$ ) as many as 8 datapoints are averaged, significantly reducing the local NETD, while in areas where datapoints are sparse, datapoints separated by more than  $0.25^\circ$  are not averaged, to prevent excessive degradation of the spatial resolution.

The distribution of resulting per-frame NETD levels is shown in Fig. 16. As for Fig. 15, the datastreams were corrected for the individual channel gains (i.e., “flat-fielded”), by a separate measurement on a reference source. The NETDs were calculated from a sequence of 150 frames acquired with a room-temperature absorber at the input of the scanner. The gain-corrected datastream then underwent the coordinate transformation described above. The rms fluctuations of the resulting 7364 image pixels (the corners of the  $128 \times 64$  image space have no data coverage) were then calculated over the 150 frames and the results mapped and histogrammed as shown. As expected, the averaging performed in the coordinate transformation somewhat reduces the NETD, though not by the full factor of  $(N_{\text{data}}/N_{\text{image}})^{1/2} = (14720/7364)^{1/2}$  that one would expect for purely random noise. The NETD distribution in the image plane illustrates that the image noise is not purely random but is rather concentrated in a relative small number of “hot pixels” that introduce high-noise ring-shaped regions into the images.

Figure 17 shows an image obtained from the camera on a human subject at the 8 m standoff distance. Again, the datastreams were calibrated on a channel-by-channel basis from a separate measurement of a reference source. However, gain variations

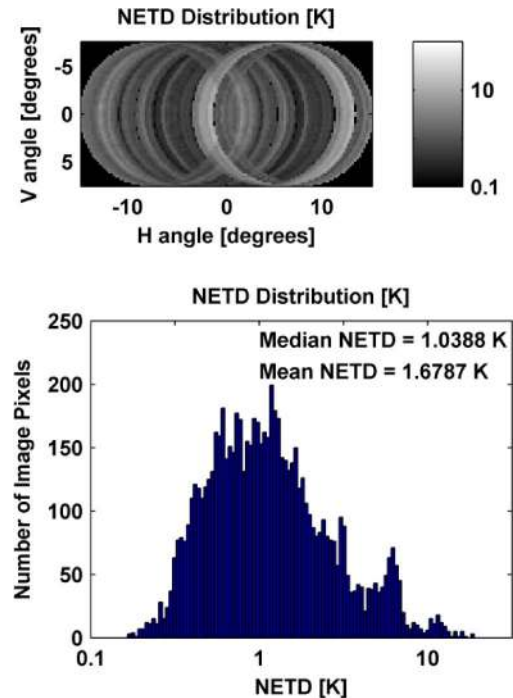


Fig. 16. (Color online) NETD distribution after coordinate transformation to image pixels (spatial map and histogram).

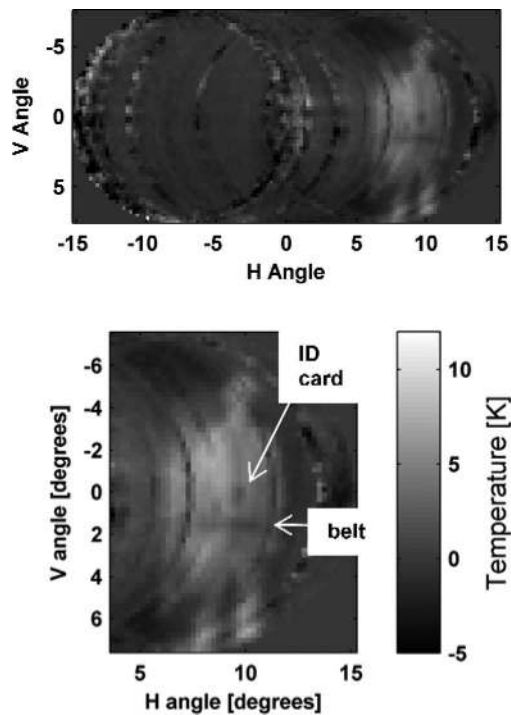


Fig. 17. Image of one of the authors at 8 m range.

between channels are still readily visible as circular stripes through areas containing significant signal. Approximately 22 min elapsed in this case, between the gain calibration and acquisition of this image. Drifts in gain and noise are clearly a significant limit on camera performance even at our current sensitivity.

An important practical question, for image processing algorithms in a security screening scenario is the degree to which the array noise can be reduced simply by averaging successive frames when viewing a stationary scene. Initially, we found that the magnitude of image fluctuations “bottomed out” for averaging times greater than  $\sim 3$  s. Temperature-induced drifts in detector bias are a natural possible source for such low frequency output fluctuations, because of the high sensitivity of output noise on detector bias. However, subsequent measurements [29] identified the source as fluctuations in stray (THz) light entering the system when the optics is imperfectly baffled. As described in Ref. [29], Allen variance measurements indicate that when well-baffled, the system output fluctuations continue to average down (consistently with white noise) out to averaging times of  $\sim 80$  s.

Figure 18 illustrates a closely related question, namely the time scale over which the gain drifts significantly. As mentioned earlier, the overall gain varies enough from channel to channel to dramatically degrade the image quality if it is not corrected for at all. The present gain calibration method, measuring the maximum signal excursion for each channel when a reference source is moved across the FOV, greatly improves the field-flatness. However, it im-

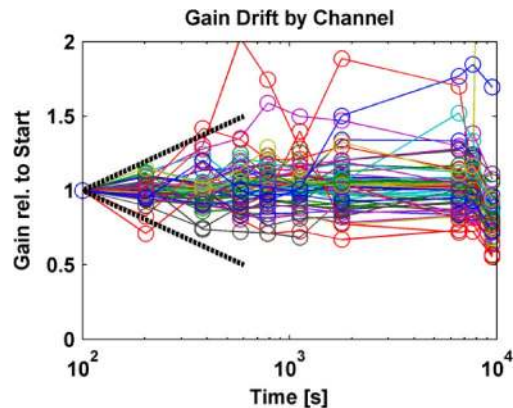


Fig. 18. (Color online) Drift in gains of all detector channels. Note the logarithmic time axis. The initial calibration was performed at  $t = 100$  s. Heavy dashed lines indicate  $\pm 50\%$  drift over 10 min.

mediately raises the question of how frequently the gains need to be remeasured in order to maintain acceptable field-flatness. The data illustrated in Fig. 18 were taken from a sequence of successive calibrations made over nearly 3 h in order to address this. The worst-case gain drift is dominated by a relatively small number of channels; for them it amounts to  $\pm 50\%$  over 10 min, as indicated by the heavy dashed lines in the figure. The great majority of the channels exhibit less serious drift, however.

## 5. Conclusion

We have described the current performance of a wideband, real-time THz camera based on a 64-element, linear focal-plane array of cryogenic microbolometers. Referred to the target plane, at 8 m range, and to a 5 fps frame rate, the median NETD of the FPA is 1.97 K averaging down for  $\sim 3$  s to  $\sim 1$  K. After the averaging involved in the coordinate transformation to the image plane, the median NETD across the field is 1.04 K. The FOV covers  $15^\circ \times 28^\circ$  ( $V \times H$ ). Sampling of the target plane is highly nonuniform because of the conical scanning geometry, and in the most sparsely sampled regions is on a  $\sim 3$  cm grid. The entire system has been demonstrated at framerates up to 10 fps, and will display the resulting imagery in real time on remote client computers. Relative to earlier raster-scanned imagery obtained with single-element, 8-element, and 16-element arrays, a major improvement in speed (more than a factor of 500 $\times$ ) and range (2 m to 8 m) has been realized. Unfortunately, the spatial resolution and sensitivity are somewhat poorer than in the earlier raster-scanned imagery. This, together with ring-shaped image artifacts associated with the accuracy and stability of gain calibration (flat-fielding) and with noise uniformity across channels, at present results in significantly poorer image quality than in the earlier systems. None of these issues is fundamental, however, and paths to improving the spatial sampling (by reconfiguring the detector module placement and the acquisition rate), and stability



(by improved baffling), while maintaining the same basic system architecture, have been identified.

The authors at VTT acknowledge Panu Helisto and Heiki Seppa for useful discussions. We are grateful to the DHS Science and Technology Directorate and the DHS Standards Office for financial support for the NIST component of this work and to the Finnish Funding Agency for Technology and Innovation (TEKES, funding decision 40306/07) for support of the VTT component.

## References

1. R. Appleby and H. B. Wallace, "Standoff detection of weapons and contraband in the 100 GHz to 1 THz region," *IEEE Trans. Antennas Propag.* **55**, 2944–2956 (2007).
2. C. R. Dietlein, A. Luukanen, F. Meyer, Z. Popovic, and E. N. Grossman, "Phenomenology of passive broadband terahertz images," in *4th ESA Workshop on Millimetre-wave Technology and Applications* (2006), pp. 405–410.
3. C. Mann, "A compact real time passive terahertz imager," *Proc. SPIE* **6211**, 6211–6214 (2006).
4. T. May, G. Zieger, S. Anders, V. Zakosarenko, M. Starkloff, H.-G. Meyer, G. Thorwirth, and E. Kreysa, "Passive standoff terahertz imaging with 1 Hz frame rate," *Proc. SPIE* **6949**, 69490C-1 (2008).
5. A. Luukanen, E. N. Grossman, A. J. Miller, P. Helistö, J. S. Penttilä, H. Sipola, and H. Seppä, "An ultra-low noise superconducting antenna-coupled microbolometer with a room-temperature read-out," *IEEE Microw. Wirel. Compon. Lett.* **16**, 464–466 (2006).
6. A. Luukanen, L. G., T. Haarnojo, P. Helisto, K. Kataja, M. Leivo, A. Rautiainen, J. Penttila, J. Bjarnason, C. Dietlein, M. Ramirez, and E. Grossman, "Passive THz Imaging system for stand-off identification of concealed objects: results from a turn-key 16 pixel imager," *Proc. SPIE* **6948**, 6948-O (2008).
7. E. N. Grossman, C. R. Dietlein, M. Leivo, A. Rautiainen, and A. Luukanen, "A passive, real-time, terahertz camera for security screening, using superconducting microbolometers," *IEEE Trans. Microwave Theor. Tech.*, 1453–1456 (2009).
8. E. N. Grossman, C. R. D., J. Chisum, A. Luukanen, J. E. Bjarnason, and E. R. Brown, "Spectral decomposition of ultra-wideband terahertz imagery," *Proc. SPIE* **6548**, 654807-1–8 (2007).
9. J. E. Bjarnason, T. L. Chan, A. W. Lee, M. A. Celis, and E. R. Brown, "Millimeter-wave, terahertz, and mid-infrared transmission through common clothing," *Appl. Phys. Lett.* **85**, 519–521 (2004).
10. A. Luukanen, L. Gronberg, P. Helisto, J. Penttila, H. Seppa, H. Sipola, C. R. Dietlein, and E. N. Grossman, "Passive euro-american terahertz camera (peat-cam): passive indoor thz imaging at video rates for security applications," *Proc. SPIE* **6548**, 65480M (2007).
11. A. Luukanen, P. Helisto, P. Lappalainen, M. Leivo, A. Rautiainen, H. Toivanen, H. Seppa, Z. Taylor, C. R. Dietlein, and E. N. Grossman, "Stand-off Passive THz Imaging at 8-meter standoff distance: results from a 64-channel real-time imager," *Proc. SPIE* **7309**, 73090F-1 (2009).
12. C. Dietlein, A. Luukanen, J. S. Penttila, H. Sipola, L. Gronberg, H. Seppa, P. Helisto, and E. N. Grossman, "Performance Comparison of Nb and NbN Antenna-coupled Microbolometers," *Proc. SPIE* **6549**, 65490-M (2007).
13. A. Luukanen and J. P. Pekola, "A Superconducting antenna-coupled hot-spot microbolometer," *Appl. Phys. Lett.* **82**, 3970–3972 (2003).
14. In superconductors,  $\kappa$  consists of contributions by the lattice phonons and the electron-like excitations called "quasiparticles". The quasiparticle contribution falls exponentially below  $T_c$ , while the lattice thermal conductivity is proportional to  $T^3$ . However, the pairing of normal metals to Cooper pairs results to a decrease of electron-phonon scattering, which can result in an *increase* in the lattice (phonon) thermal conductivity. Thus, the behavior of  $\kappa(T)$  is very material dependent and beyond the scope of this paper.
15. H. Merkel, P. Khosropanah, D. W. Floet, P. A. Yagoubov, and E. L. Kollberg, "Conversion gain and fluctuation noise of phonon-cooled hot-electron bolometers in hot-spot regime," *IEEE Trans. Microwave Theory Tech.* **48**, 690–699 (2000).
16. D. P. Neikirk and D. B. Rutledge, "Air-bridge microbolometer for far-infrared detection," *Appl. Phys. Lett.* **44**, 153–155 (1984).
17. K. D. Irwin, "An application of electrothermal feedback for high resolution cryogenic particle detection," *Appl. Phys. Lett.* **66**, 1998–2000 (1995).
18. J. C. Mather, "Bolometer noise: nonequilibrium theory," *Appl. Opt.* **21**, 1125–1129 (1982).
19. J. P. Penttila, H. Sipola, P. Helisto, and H. Seppa, "Low-noise readout of superconducting bolometers based on electrothermal feedback," *Supercond. Sci. Technol.* **19**, 319–322 (2006).
20. D. B. Rutledge, D. P. Neikirk, and D. P. Kasilingham, "Integrated circuit antennas," in *Infrared and Millimeter Waves*, Vol. 10, K. J. Button, ed. (Academic, 1983), pp. 1–90.
21. C. R. Dietlein, J. D. Chisum, M. D. Ramirez, A. Luukanen, E. N. Grossman, and Z. Popovic, "Integrated Microbolometer Antenna Characterization from 95–650 GHz," *International Microwave Symposium Digest*, 1165–1168 (2007).
22. A. Tamminen, J. Ala-Laurinho, J. Mallat, A. Luukanen, E. N. Grossman, and A. Raisanen, "Characterization of Antenna-coupled Microbolometers for THz Imaging," presented at the 5th ESA Workshop on Millimetre Wave Technology and Applications and 31st ESA Antenna Workshop, ESTEC, Netherlands, 2009.
23. D. F. Filipovic, G. P. Gauthier, S. Raman, and G. M. Rebiez, "Off-axis properties of silicon and quartz dielectric lens antennas," *IEEE Trans. Microwave Theory Tech.* **45**, 760–766 (1997).
24. E. N. Grossman, C. R. Dietlein, J. E. Bjarnason, M. D. Ramirez, M. Leivo, J. Penttila, P. Helisto, and A. Luukanen, "Imaging with modular linear arrays of cryogenic nb microbolometers," *Proc. SPIE* **6948**, 694806 (2008).
25. D. M. Sheen, T. E. Hall, R. H. Severtsen, D. L. McMakin, B. K. Hatchell, and P. L. J. Valdez, "Active Wideband 350 GHz Imaging system for concealed weapon detection," *Proc. SPIE* **7309**, 73090-I, 2009.
26. N. M. Vaidya and T. Williams, "A novel approach to automatic threat detection in mmw imagery of people scanned in portals," *Proc. SPIE* **6948**, 69480F-1 (2008).
27. J. C. Lagarias, J. A. Reeds, M. H. Wright, and P. E. Wright, "Convergence properties of the nelder-mead simplex method in low dimensions," *SIAM J. Optimization* **9**, 112–147, 1998.
28. C. R. Dietlein, Z. Popovic, and E. N. Grossman, "Aqueous blackbody calibration source for millimeter-wave/terahertz metrology," *Appl Optics* **47**, 5604–5615 (2008).
29. A. Luukanen, L. Gronberg, M. Gronholm, P. Lappalainen, M. Leivo, A. Tamminen, J. Ala-Laurinaho, C. R. Dietlein, and E. N. Grossman, "Real-time passive terahertz imaging system for standoff concealed weapons imaging," *Proc. SPIE* (to be published).